Jupiter's Tropospheric Thermal Emission II: Power Spectrum Analysis and Wave Search

JOSEPH HARRINGTON[1] AND TIMOTHY E. DOWLING

Department of Earth, Atmospheric, and Planetary Sciences, Room 54-410, Massachusetts Institute of Technology, Cambridge, Massachusetts 02139

AND

RICHARD L. BARON

Institute for Astronomy, University of Hawai'i, Honolulu, Hawai'i 96822

Revision 1.2 submitted to *Icarus* 30 June 1995.
Revision 2.1 submitted to *Icarus* 18 March 1996.
Revision 3.2 submitted to *Icarus* 19 June 1996.

---

[1]Current address:
Code 693
Goddard Space Flight Center
Greenbelt, MD 20771-0001
E-mail: jh@tecate.gsfc.nasa.gov

Pages: 31 excluding figures, tables, and cover
Figures: 5
Tables: 2

Keywords: ATMOSPHERES, DYNAMICS, Jupiter; CLOUDS, Jupiter; INFRARED OBSERVATIONS, Jupiter; JOVIAN PLANETS, Atmosphere; JUPITER, ATMOSPHERE, Dynamics

Proposed running heads:
Left: Harrington, Dowling, and Baron
Right: Jupiter 5-μm Imaging: Power Spectrum and Wave Search

Address correspondence and proofs to:
Joseph Harrington
Code 693
Goddard Space Flight Center
Greenbelt, MD 20771-0001
(301) 286-9130
(301) 286-0212 fax
jh@tecate.gsfc.nasa.gov

We study power spectra and search for planetary waves in images of Jupiter's cloud opacity. The observation wavelength of 4.9 μm senses thermal emission from the ∼5-bar level; overlying clouds attenuate the emission. Our companion paper (J. Harrington *et al.* 1996, *Icarus*, in press) describes 19 nights of observations (6 with 360° longitude coverage) and new reduction techniques. Atmospheric seeing limits resolution to ∼2,500 km. Zonal power spectral density at planetary wavenumbers higher than ∼25 follows a power law in the wavenumber. Eastward jets average -2.71±0.07 and westward jets, excluding cloud-obscured regions, average -3.14±0.12. Wavenumbers 1 – 24 roughly follow power laws near -0.7 for both jet directions, but with many superposed discrete features. The meridional spectrum similarly breaks around wavenumber 25, with power law trends of -0.36 and -3.27. However, a pattern of undulations is superposed over its linear trends.

Editor: replace ''Icarus, in press'' with the actual publication reference in this issue of the journal.

L. D. Travis (1978, *J. Atmos. Sci.* 35, 1584–1595) established an empirical correspondence between power spectra of atmospheric kinetic energy and of cloud opacities for the Earth and analyzed Venus cloud data under this assumption. We do the same for Jupiter. If the Rossby deformation radius, L_d, were an energy input scale, as baroclinic instability theory predicts, one would expect energy and enstrophy cascades (power laws

of -5/3 and -3, respectively) on opposite sides of the wavenumber corresponding to L_d. If the top of our high-wavenumber power law is L_d, its value is ∼2,100 km at 45° latitude.

Our spectra show persistent features with phases moving linearly over the 99-day observation period. Some of these can be identified with periodic features such as vortex chains and the equatorial plumes. The origin of others is less certain. We present a table of our best wave candidates.

INTRODUCTION

Jupiter's middle and deep atmospheric regions strongly influence the types of dynamics that occur above them (Dowling and Ingersoll 1989). The direct study of these regions is inhibited by the presence of the ammonia clouds, which reflect most visible wavelengths and whose tops are located near 250 mbar (West *et al.* 1986). The deepest-probing light we can receive from Jupiter is thermally emitted near the 5-bar level at wavelengths close to 5 μm (Kunde *et al.* 1982). This light is attenuated as it passes through the various cloud layers, giving us our best source of information on the optical thicknesses of the clouds. Although spectral and photometric work at this wavelength has been progressing for some time (Beer and Taylor 1973, Terrile 1978), only in the past decade have electronic infrared imagers achieved the sensitivity and spatial resolution necessary for studies of the horizontal variation of Jupiter's cloud opacities at this wavelength.

The first paper in this series (Harrington *et al.* 1996, hereafter Paper I) describes the acquisition of maps of Jupiter's cloud opacities on 19 nights between January and April of 1992. The maps were taken at a wavelength of 4.9 μm with the ProtoCAM instrument at the NASA Infrared Telescope Facility. On six of these nights we obtained complete longitude coverage. Although there is much work at optical wavelengths involving the tracking of features and winds on Jupiter (Limaye 1986, Beebe *et al.* 1980), the present work concentrates on the power spectrum of Jupiter's cloud opacities. The next section provides background information about the use of power spectra in terrestrial atmospheric dynamics and briefly reviews other observations of planetary waves on Jupiter. We then use our power spectra to characterize the statistics of cloud patterns on Jupiter, to investigate the length scales of energy deposition, and to search for planetary-scale waves. We conclude with interpretation and considerations for future observations.

Background

In this paper we use the power spectrum in two different ways: as a statistical tool for studying the distribution of power across Fourier components and as a device for identifying strong periodic activity at discrete wavenumbers. The practical goal of a general power spectrum analysis is to find a compact analytical expression, such as a power law, that captures the statistics of a cloud field over a large range of scales. Such a description provides a diagnostic tool that can reveal input scales of energy and can quantify the type of turbulence acting in the atmosphere. A compact description would also allow the effects of cloud dynamics to be incorporated in global radiative-transfer calculations in an efficient manner.

In recent years traditional power spectrum analyses of Earth's cloud variability have given way to structure-function techniques that connect directly to theories of tracer advection in two- and three-dimensional (2D and 3D) flows and on the fractal nature of the resulting patterns (Tessier *et al.* 1993, Pierrehumbert 1994). Although progress in this area is rapid, the problem of cloud patterns is complex, and the tools for data analysis are still evolving. This paper is an initial foray into the field using Jupiter data, so we have elected to keep the analysis simple and traditional.

Our goal is to determine over what wavenumber ranges a power-law description of the power spectrum of Jupiter cloud opacity is accurate and to determine the corresponding exponents. In the literature, even this traditional analysis suffers from sizeable gaps between theory and observation. For example, cloud opacities may act as passive tracers. Pierrehumbert (1994) and co-workers have studied power laws stemming from tracer mixing processes. Jupiter's small number of large vortices argues in favor of 2D turbulence. Simple dimensional arguments predict that a passive 2D tracer that is freely evolving in homogeneous, isotropic turbulence without dissipation will have a k^{-1} spectrum, where k is the wavenumber (Batchelor 1959). However, this idealized spectrum is not often observed. Pierrehumbert (1992) shows that the Batchelor spectrum is inheriently transient and as the system approaches homogeneity the spectrum becomes non-universal, depending on both the initial conditions and on the large-scale flow geometry. Generally speaking, as patches of the fluid become homogenized with the tracer, the discontinuities of the patch edges lead to a steeper k^{-2} spectrum, as shown by Saffman (1971). Pierrehumbert (1994) examines high-resolution 2D turbulence simulations and finds that passive tracers tend to exhibit a power law intermediate between k^{-1} and k^{-2}.

But some observations of cloud opacities, for example those of Travis (1978) and also of the present work, exhibit a k^{-3} spectrum. If not a passive tracer, then what sort of field is cloud opacity? The most notable characteristic of 2D turbulence is that energy cascades to large scales instead of small scales (Charney 1971, Danilov *et al.* 1994). In other words, 2D vortices merge rather than fall apart like a smoke ring. In so doing, the vortices continuously wrap and stretch long filaments, such that the enstrophy (squared vorticity, a measure of filamentation) cascades to small scales. Unlike a passive tracer, the kinetic energy spectrum behaves as k^{-3} in the wavenumber range over which enstrophy is cascading. If there were a certain wavenumber for energy input, as one would expect if baroclinic instability were operating (see Power Spectrum Analysis, below) then for wavenumbers smaller than this input scale the power spectrum of kinetic energy would show the well-known $k^{-5/3}$ Kolmogorov scaling, whereas the larger wavenumbers would show a k^{-3} power law. If significant energy were input at additional wavenumbers, the up- and down-scale cascades would interfere with one another and destroy the simple power law between the input wavenumbers.

Kinetic energy fields come from velocity measurements, but power-spectrum analysis requires accuracies much better than the $\sim$5 m/sec uncertainties of data for planets other than the Earth (Sada *et al.* 1996, Travis 1978). Mitchell (1982) and

Mitchell and Maxworthy (1985) carried out such a study using the Voyager wind data, with large scatter in the resulting power spectra. For Earth, Travis found a close correspondence between power spectra of Earth's atmospheric kinetic energy and power spectra of its visible and infrared cloud intensities. His cloud data come from a Mariner 10 image (λ_{eff}=0.578 μm), five pairs of visible (0.55 – 0.75 μm) and thermal infrared (10.5 – 12.6 μm) images from the SMS-1 satellite, and one such pair from the GOES-1 satellite. Travis's Fig. 5, reproduced here in Fig. 1, shows a solid line for the cloud brightness spectrum and circles for various kinetic energy spectra (see caption). The important result for the present work is that cloud intensity spectra agree with kinetic energy spectra in each of two latitude regions, even though the kinetic energy spectra in the two regions are different from each other. Assuming that the correspondence held for Venus as well, Travis used cloud-intensity spectra as a surrogate for kinetic energy spectra. Below, we offer interpretations of our observational results under the same assumption.

Travis's assumption is controversial. We have been unable to derive ourselves or find in the literature a plausible reason why power laws in kinetic energy power spectra should appear in cloud opacity power spectra with the same exponent. Although we do not solve this problem, we add to the discussion by showing that the Jupiter data, like the Earth and Venus data examined by Travis, exhibit a kinetic-energy-like exponent of -3 over a wide range of wavenumbers.

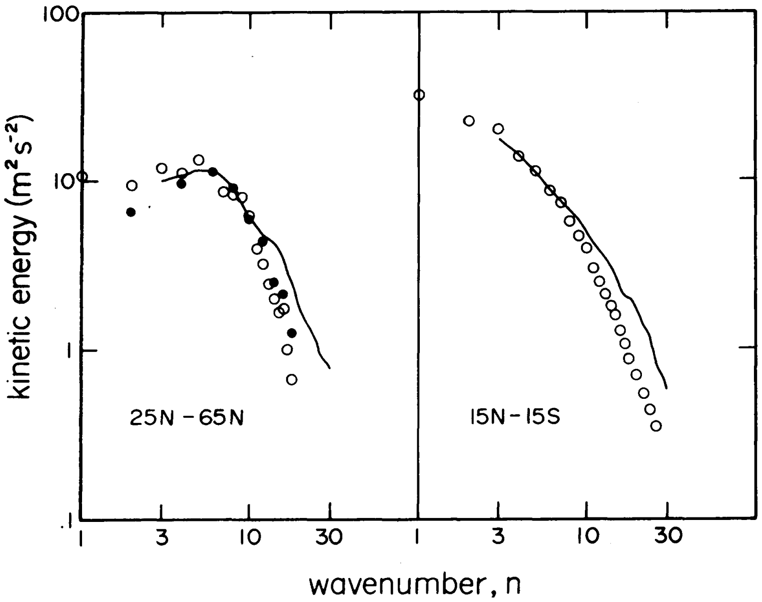

Fig. 1. Comparison of Earth kinetic energy power spectra (circles) and cloud intensity spectra (lines) from Travis (1978). Open circles are from wind data sensitive to 200 mbar at a single latitude. Filled circles are from winds at 200, 500, and 850 mbar at two discrete latitudes. The circles are normalized to match each other at n=6, which Travis identifies as the scale of the deformation radius for Earth. The lines are an average of power spectra derived from 12 Earth images at a variety of visible and infrared wavelengths. The spectrum from each of the Earth images is an average of its zonal spectra over the indicated latitude region. In spite of the clearly different forms taken by the power spectra at different latitudes, the two different measurements agree on the basic form in both regions. Reproduced from *Journal of the Atmospheric Sciences.*

Even more than as a statistical tool, the power spectrum is familiar as a means for identifying discrete periodicities in data. Propagating waves that manifest themselves in cloud opacities and chains of periodic vortices would both appear as discrete peaks in a zonal power spectrum, and we use our spectra to search for such features. A previous wave search with data from the Voyager Infrared Interferometer Spectrometer (IRIS) at this wavelength (Magalhães *et al.* 1990) yielded null results. However, the present study has ten times the linear spatial resolution and six times the temporal resolution of the spacecraft study.

Global, periodic, thermal features are apparent in infrared observations of Jupiter's stratosphere and upper troposphere at other wavelengths (Magalhães *et al.* 1989, 1990); these features move slowly with respect to the interior rotation rate (System III). Deming *et al.* report activity at 20° N. Magalhães *et al.* (1989, 1990) report thermal waves at 15° N, planetary wavenumber 9, 270 mbar and 20° N, wavenumber 11, in 45-μm cloud opacities. Orton *et al.* (1991) report a wave moving no faster than ±30 m/s at 22°N, 30 mbar. Saturn sports a circumpolar hexagonal feature (Godfrey 1988), which is apparent in Voyager images, and IRIS data reveal Rossby waves at wavenumber 2 between 20° N and 40° N at 130 mbar (Achterberg and Flasar 1996). The hexagon has also been interpreted as a Rossby wave (Allison *et al.* 1990). The slow thermal features are encouraging and lead us to a general search for such features in Jupiter's tropospheric cloud opacities. A dispersion relation derived empirically from a family of observed Rossby waves would greatly constrain studies of the stability of Jupiter's zonal jets (Dowling 1995, especially Eq. 34), as well as other aspects of atmospheric dynamics.

We note that the visibly-prominent equatorial plumes may be only distantly related to these features. Thought to be convection sites, they move quickly with respect to System III and have a different appearance from both the features on Saturn and those seen in the infrared on Jupiter. Allison (1990) has suggested that conditional instabilities associated with deep waves drive the convection that makes the features visible.

The existence of a family of waves that move slowly relative to the presumed internal planetary rotation period implies a mechanism whereby the dynamics of the stratosphere and upper troposphere are tied, possibly indirectly, to the deep interior. Hart *et al.* (1986a,b) have proposed one possible mechanism: a pattern of convection cells in the planetary interior, the top of which form a fluid velocity pattern static in the rest frame of the interior. They simulate the interior convection of the giant planets both by numerical methods and by means of a physical model flown in space. For rapidly-rotating spheres with a purely radial temperature gradient, these models form narrow convection cells that each extend from pole to pole but cover only a few tens of degrees in longitude. If this "banana-cell" pattern of alternating upward and downward velocity were strong enough, it could affect the effective thickness of the troposphere and act as a forcing or selection mechanism for Rossby waves. Such a pattern might give rise to waves stationary in the rest frame of the cells and having planetary wavenumbers related to the number of convection cells. Meridionally-aligned features might also result. Detection of a strong convection pattern underlying the weather layer would begin to address the question of what ties Jupiter's zonal wind system and stratospheric thermal waves to the rotation rate of the deep interior. Such meridional coherence across latitudes does not in fact appear in our data, but we do have positive detections of a number of waves at particular latitudes, as discussed below.

POWER SPECTRUM ANALYSIS

To derive power spectra of Jupiter's cloud opacities, we extracted 1°-wide latitude strips from our 19 composite maps (for examples from two different nights, see left panel of Fig. 2 and Fig. 2 of Paper I). We calculated the power spectral density (PSD) with Lomb normalization following Press *et al.* (1992, pp. 575–584). The spectral image (center panel of Fig. 2) was produced by averaging the spectra at each latitude over the 19 nights and stacking the resulting average spectra. This image has coordinates of wavenumber and latitude and pixel values of normalized PSD. Although mosaicking and compositing errors leave systematic patterns in the individual spectra (see Fig. II.3 of Harrington 1994), these effects are eliminated from practical concern by averaging over the 19 nights.

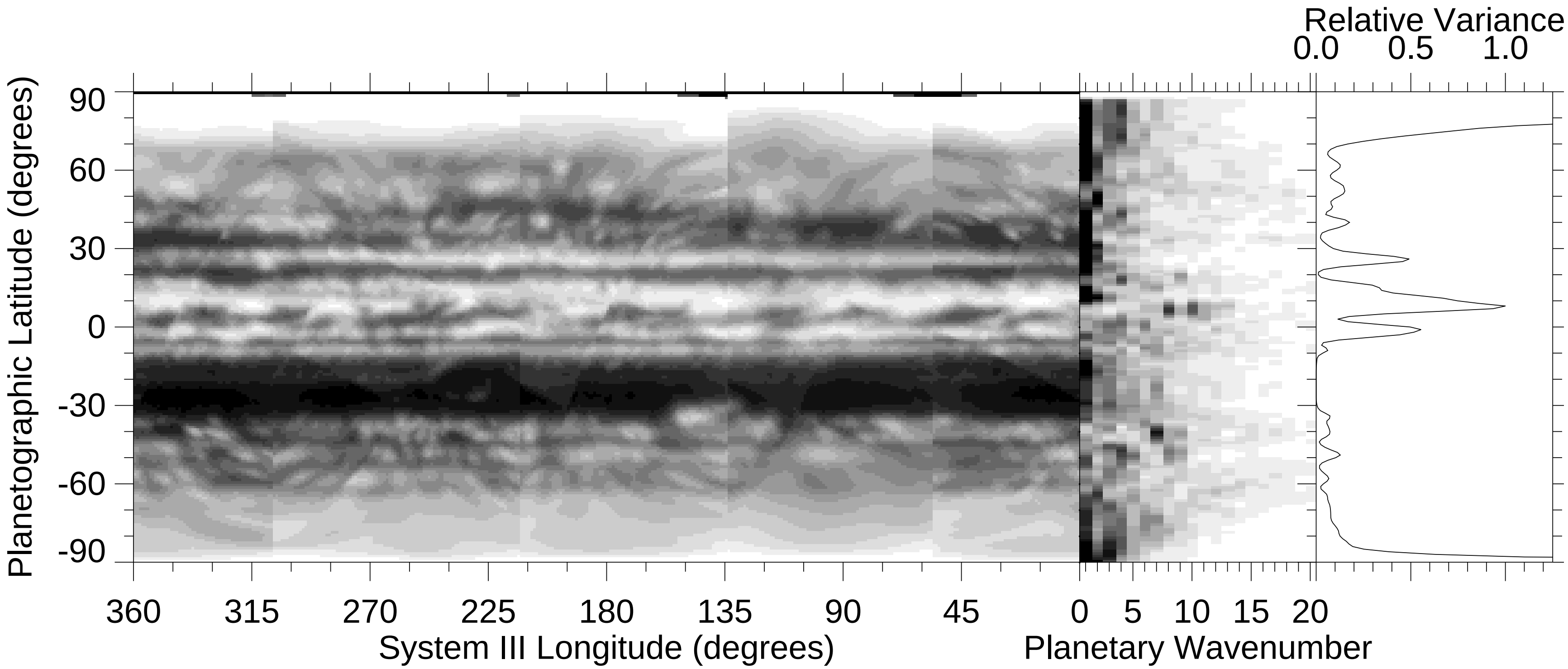

Fig. 2. 4.9-µm map of Jupiter on 27 February 1992 (left), average zonal power spectrum for all 19 nights (center), and relative zonal variance of map intensities (right). Dark features indicate high cloud opacity in the map and high power spectral density in the spectrum. The stretch is logarithmic in intensity in the left panel and linear in the center. The equatorial plumes are prominent in the map. The Great Red Spot is at latitude -20°, longitude 240° and is mostly obscured by clouds at this time and wavelength. Structure at latitudes poleward of 60° suffers in map projection. Each horizontal row in the power spectrum is the average of Lomb-normalized spectra for the adjacent map latitude for all 19 nights. The normalization (see text) is proportional to the variance plotted for each latitude in the right panel, and is used to compare spectra at different latitudes and to search for discrete waves. Many of the brightest features in the power spectrum correspond to periodic features whose phase changes linearly with time (see Fig. 5 and Table II). Figure 2 of Paper I contains a different night's map, for comparison.

The Lomb method has several advantages over the simple fast Fourier transform (FFT) algorithm (see Press *et al.*, pp. 496–536, and elsewhere). First, it allows comparison of one spectrum to another even at very different intensity levels. Second, it directly indicates the significance of the values in the spectrum. Third, the data need be neither contiguous nor evenly sampled. Even though our maps are evenly-sampled representations of the original image data, not all nights have full coverage. Fourth, one can specify the (not-necessarily-integral) wavenumbers of interest rather than accepting the set provided by the FFT. Using the Lomb method allowed us to specify the same spatial frequencies in the incomplete maps as in those with complete coverage, and thus to average the power spectra from all 19 nights. The Lomb method has two disadvantages: First, it gives no phase information. However, this is easily obtained for a limited number of frequencies by fitting a sinusoid of the desired period to the data. Second, it is slower, being composed of two FFT operations and some additional processing.

As a check on our use of the Lomb technique, we derived power spectra with integral planetary wavenumbers for each 1° strip of latitude on the nights with 360° maps using both the Lomb and the FFT methods. We converted the FFTs to Lomb periodograms by squaring the FFT amplitudes to derive power spectra, multiplying by the number of data points, and dividing by the variance of the data. The average fractional difference, $|(a-b)/(a+b)|$, between the two sets of amplitudes is $\sim 10^{-6}$ or less for wavenumbers below our spatial resolution cutoff of ~ 70 and 10^{-3} or less for all wavenumbers except a few very close to the Nyquist frequency.

Figure 3 presents the averaged power spectra of latitudes contained in the eastward and westward zonal jets, a meridional spectrum averaged over all longitudes and nights (5,334 averaged spectra), and an individual spectrum from a single latitude strip on a single night, to give a sense of the raw spectra. For most latitudes within the $\pm 60^{\circ}$ limits of good map projection, plotting the logarithm of the power spectrum against the logarithm of the planetary wavenumber (m) reveals a slope near -0.8 at low wavenumbers with superposed discrete features, a steeper slope at wavenumbers higher than $\sim$25 that is relatively linear, and a low-intensity tail starting at $m\sim 70$, whose slope and curvature vary. Averaging over latitudes significantly reduces noise and reveals the underlying structure more clearly. The meridional spectrum is provided to illustrate the spectral behavior of the zonal intensity including the cloud belts. The belt-zone intensity variation is characterized not by a single peak but rather by a series of steadily-weakening peaks.

Table I reports fits to linear ranges of the spectra averaged over regions noted in the table. We evaluated the point between the two slopes by eye, and found that in most of the narrow latitude ranges the breakpoint was within 1 or 2 wavenumbers of 26. We adopted this value and terminated the fits 2 wavenumbers away. Each average includes only those wavenumbers within the resolution limit, which varies with latitude (see below). The highest wavenumbers have representation only from the lowest

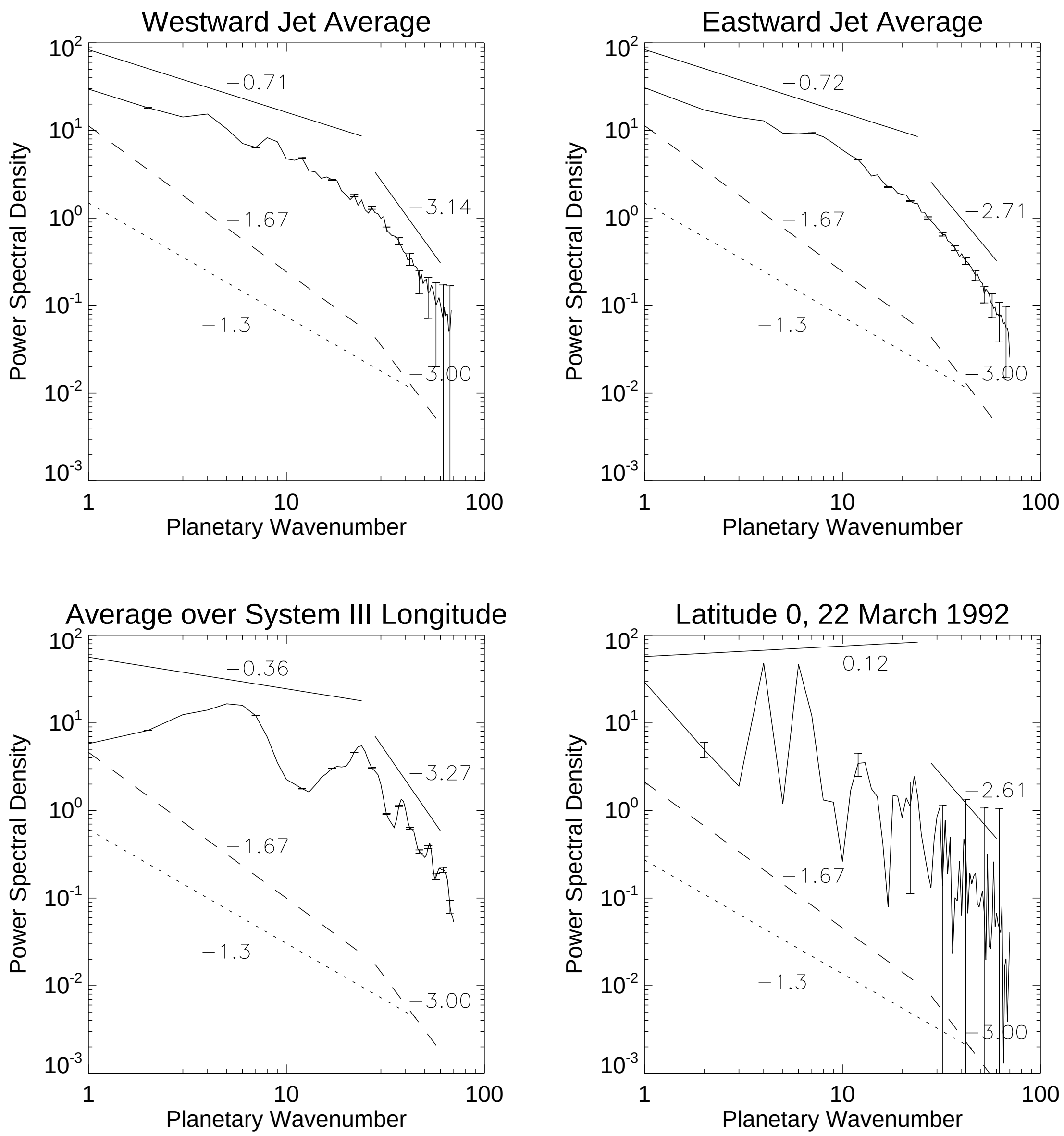

Fig. 3. Power spectrum averages. Power-law fits in the indicated wavenumber ranges are above the data. Dashes plot the theoretical 2D energy and enstrophy cascade slopes. Mitchell and Maxworthy (1985) measured slopes of -1.3 (a portion is plotted with dots) and -3 in wind velocity data, but with a breakpoint near wavenumber 45. The lower left plot is a meridional spectrum. It has similar trends to the zonal spectra, but with a superposed pattern of peaks. This plot uses the same spatial wavenumbers as the zonal plots (but see text). The lower right plot is from a single night at a single latitude, to show the quality of unaveraged spectra. See text for discussion of errors. At high wavenumbers, the zonal spectra confidently follow power laws with slopes near -3, but discrete waves disrupt the linearity of the low-wavenumber spectra. See Table I for numerical fit values.

latitudes in an average, hence the growth of error bars at the highest wavenumbers. The upper limit for the high-wavenumber fit is the highest wavenumber resolved in the average. The width of our image point-spread function (PSF) corresponds to about 2° on Jupiter, and this is roughly equivalent to the smoothing performed by Travis to eliminate an aliasing problem from abrupt cloud edges in his data for the Earth. We found that smoothing the data to reduce noise also reduced our sensitivity at high wavenumbers. We have therefore not further smoothed our data, nor have we rebinned their intensities. We also take linear rather than log averages. Although Travis averages in the log, the Fourier transform is linear and other workers (*e.g.,* Mitchell and Maxworthy 1985, Mitchell 1982, and Julian and Cline 1974) do not mention log averaging. These averages presume that the spectra are constant over the 19 nights and within the averaging region, which is a prediction of cascade theory for inertial subranges (see Background, above).

We wish to search for waves and establish power laws in the presence of potentially many types of signals. We use the variance of the data to place an upper bound on random meteorological noise. Because the variance of a data set consisting of Gaussian random noise is proportional to the standard deviation of its exponentially-distributed, white-noise power spectrum, the Lomb periodogram is normalized according to the data's variance. Significant peaks in the data appear at PSD levels larger than unity, so one assigns uncertainties of unity to the points in the individual power spectra.

TABLE I
Power Law Fits to Regions of the Spectra

Latitude Range °	Planetary Wavenumber Range	Power[a] Law Fit	Planetary Wavenumber Range	Power Law Fit	Conf. (%)
Averaged Eastward Jets:					
various	1 – 24	-0.720 ± 0.001	28 – 60	-2.709 ± 0.07	99.6
Averaged Westward Jets:					
various	1 – 24	-0.715 ± 0.001	28 – 60	-3.137 ± 0.12	92.2
Meridional[b]:					
0.0 – 360.0	1 – 24	-0.361 ± 0.001	28 – 60	-3.271 ± 0.01	0.0
Representative unaveraged spectrum from 22 March 1992:					
-0.5 – 0.5	1 – 24	0.118 ± 0.022	28 – 60	-2.605 ± 3.11	100.0
Regional Averages:					
34.5 – 60.5	1 – 24	-0.862 ± 0.001	28 – 59	-2.852 ± 0.12	100.0
-15.5 – 35.5	1 – 24	-0.800 ± 0.001	28 – 60	-2.640 ± 0.08	99.8
-35.5 – -14.5	1 – 24	-0.637 ± 0.001	28 – 60	-2.699 ± 0.14	99.8
-60.5 – -34.5	1 – 24	-0.408 ± 0.001	28 – 59	-2.920 ± 0.11	98.6
Individual Zonal Jets:					
54.5 – 58.5	1 – 24	-0.826 ± 0.003	28 – 42	-3.212 ± 0.57	93.7
49.5 – 54.5	1 – 24	-0.639 ± 0.003	28 – 47	-3.168 ± 0.33	78.5
45.5 – 49.5	1 – 24	-0.823 ± 0.003	28 – 50	-3.171 ± 0.27	58.8
44.5 – 45.5	1 – 24	-0.682 ± 0.006	28 – 51	-2.195 ± 0.48	99.9
41.5 – 44.5	1 – 24	-0.752 ± 0.003	28 – 54	-2.814 ± 0.32	82.5
38.5 – 41.5	1 – 24	-1.019 ± 0.003	28 – 56	-3.530 ± 0.35	92.0
33.5 – 38.5	1 – 24	-1.031 ± 0.003	28 – 59	-2.368 ± 0.18	100.0
29.5 – 33.5	1 – 24	-1.082 ± 0.003	28 – 60	-2.474 ± 0.22	98.7
19.5 – 29.5	1 – 24	-1.336 ± 0.002	28 – 60	-2.459 ± 0.21	100.0
15.5 – 19.5	1 – 24	-0.478 ± 0.003	28 – 60	-3.118 ± 0.26	88.3
-15.5 – 16.5	1 – 24	-0.574 ± 0.001	28 – 60	-2.709 ± 0.11	100.0
-23.5 – -15.5	1 – 24	-0.700 ± 0.002	28 – 60	-2.419 ± 0.19	98.6
-31.5 – -23.5	1 – 24	-0.567 ± 0.002	28 – 60	-2.856 ± 0.26	100.0
-34.5 – -31.5	1 – 24	-0.516 ± 0.003	28 – 60	-3.525 ± 0.61	100.0
-47.5 – -34.5	1 – 24	-0.252 ± 0.002	28 – 59	-2.269 ± 0.15	94.8
-50.5 – -47.5	1 – 24	-0.270 ± 0.004	28 – 49	-3.070 ± 0.47	99.4
-56.5 – -50.5	1 – 24	-0.530 ± 0.003	28 – 46	-3.339 ± 0.24	65.4
-59.5 – -56.5	1 – 24	-0.517 ± 0.004	28 – 40	-3.100 ± 0.30	0.0

[a] Confidences for low-wavenumber fit are all less than 0.05%. These fits are presented to characterize the first-order behavior of the region, not to establish power laws.
[b] Longitude range stated, same spatial wavenumbers as in zonal fits.

Observational error in these data is small, about 1/200 of the typical zonal variance. Further, it is dominated by nearly constant background and array readout noise sources, rather than by the variable photon statistics of Jupiter. Thus, these uncertainties propagate into the power spectrum as a low level of nearly-white noise. Of greater concern are the effects of mosaicking and mapping errors (see Paper I). Our composite images rarely contain pixels more than 45° from the central meridian and never use pixels further than 60° away. If we simulate gross mosaicking/mapping errors by shifting 25% of the dataset by 1° (much more than we expect for such a large fraction of the data), the fractional leakage to the adjacent wavenumber is about 1.6×10^{-5} at wavenumber 1, 0.15% at wavenumber 10, 1.4% at wavenumber 30, and 4.2% at wavenumber 50. Leakages 2 wavenumbers away are about half these values. Two 1° shifts in opposite directions, the second representing about 10% of the data, yield numbers well under twice these values. For our power spectra, these effects are all tiny compared to the variance. When we average over 19 nights and over a range of latitudes, even the variance effects of a single night are made small.

Since we are fitting in the log, we have weighted the uncertainties by 1/PSD. We calculate the confidence (probability that chi squared as poor as that calculated from the data would occur by chance from the fitted power law) to test the presumption of quiescent spectrum as well as the validity of the power-law models of the fits. The high-wavenumber fits, with one exception, all have moderate to excellent confidence (some greater than 99.95%), so we conclude that the underlying behavior is in fact linear in this subrange.

The confidences at low wavenumbers and in both meridional subranges are all less than 0.05%, indicating that the constant power-law model is not valid here. In an effort to find a linear region corresponding to the -5/3 energy cascade, we attempted fits in the low-wavenumber region starting at wavenumbers as high as 12 (higher than those of all wave candidates in Table II). Those fits still had vanishing confidence, and also had a large distribution in their slopes. We present the low-wavenumber and meridional fits only to characterize the first-order behavior of the spectra and do not draw any further conclusions from them. Note that the spectral breakpoint is close to the location (PSD=1) where the Lomb-normalization predicts significant wave activity. In a region with waves the inertial assumption of cascade theory breaks down, and we do not expect simple power laws. See Wave Search, below, for statistics on some individual wavenumbers over time.

Three dynamical parameters potentially affect the ends of the actual subranges. These are the radius of deformation, the Rhines cascade-arrest scale, and the Rossby number. In addition, image quality alters the observed spectrum at high wavenumbers. Figure 4 shows these parameters and where they appear relative to each other and the data.

First, image quality (atmospheric "seeing", optical diffraction, telescope tracking

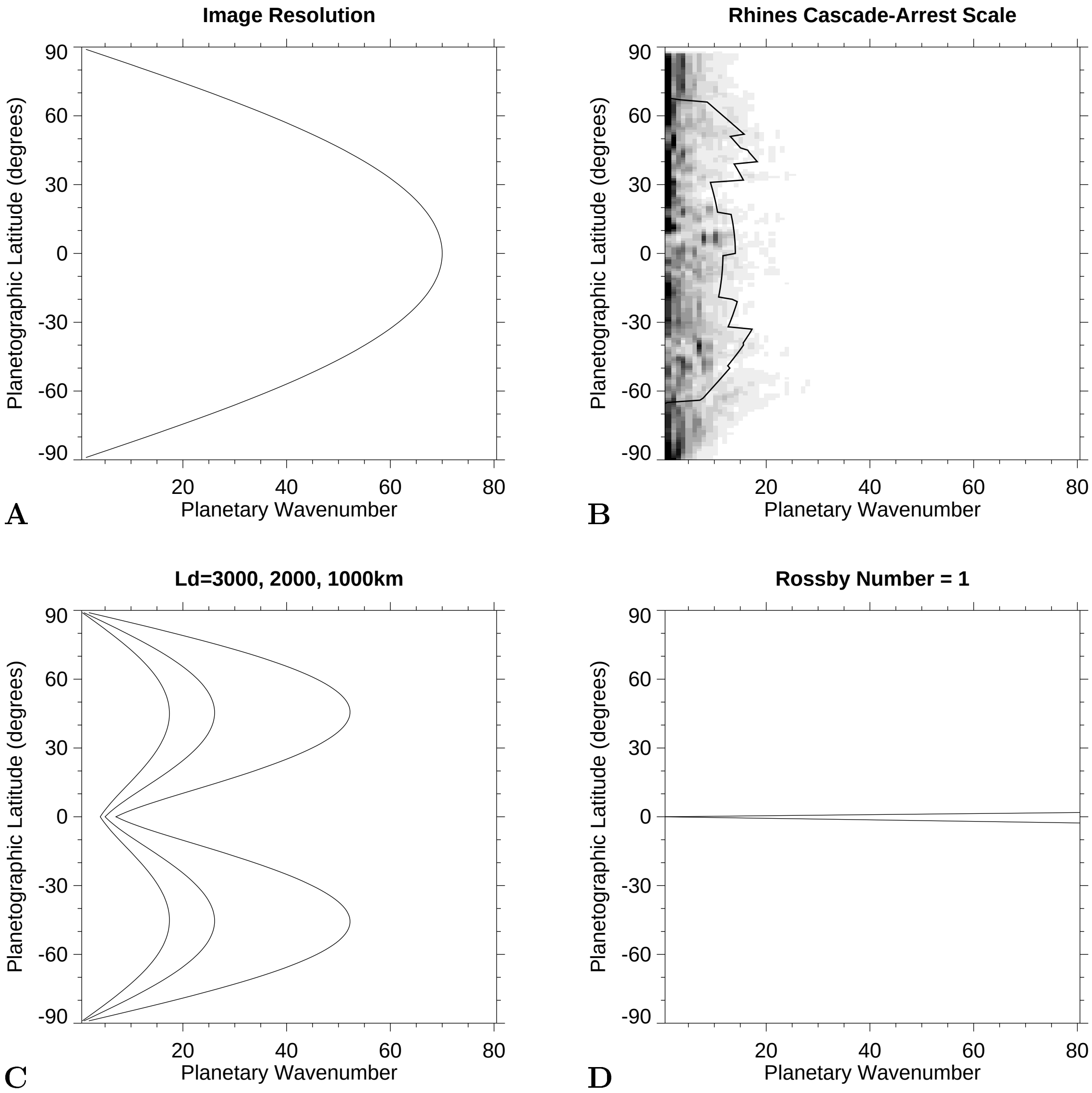

Fig. 4. Scales that affect the observed spectra as a function of latitude. Panel **A** shows the effect of image resolution on our sensitivity to high wavenumbers; because a circle of longitude is smaller at high latitude, planetary wavenumber sensitivity decreases there. Panel **B** shows the Rhines cascade-arrest scale (see Eq. 1) plotted over the spectral image of Fig. 2, to show how the plotted limit relates to the region of the data where discrete waves appear (see Fig. 3 for overall spectral appearances). Panel **C** shows the location of three possible values for the deformation radius, L_d; from left to right these are 3,000, 2,000, and 1,000 km at 45° latitude, assuming gravity-wave speed is independent of latitude. Panel **D** shows the wavenumber where the Rossby number equals unity; values are smaller poleward of the wedge and larger within it. See text for further discussion.

errors, etc.) places a fundamental limit on how small an object the images resolve. The full-width at half-maximum (FWHM) of the PSF in the images is typically $0\farcs5$–$0\farcs75$ and has a greater effect away from the sub-Earth point on the planet than near it. Seeing acts much like a Gaussian filter. To find its effect on power spectra, we convolved sine curves with Gaussian curves of the appropriate width. We find that at Jupiter's equator a $0\farcs75$ FWHM PSF reduces the amplitude of the power spectrum at planetary wavenumber 60 by 50%. As latitude increases, this limit moves to lower wavenumbers, as shown in Fig. 4A. $0\farcs75$ corresponds to ~2,500 km at Jupiter's distance, which allows us to be sensitive to values of the Rossby deformation radius, L_d, as small as $2,500$ km$/2\pi \approx 400$ km.

Second, if a cascade reaches sufficiently low wavenumbers, energy can propagate away in Rossby waves. This energy sink destroys a cascade's inertial character and terminates the linear portion of its power spectrum. The lower-limit wavenumber for turbulence in geostrophic systems is the Rhines cascade-arrest scale (Rhines 1979, Shepherd 1987),

$$k_\beta = \sqrt{\frac{\beta}{2U}}, \tag{1}$$

where U is the horizontal wind velocity scale, $\beta = 2\Omega\cos(\lambda)/R$ is the local derivative of the vertical component of the Coriolis parameter, $f = 2\Omega\sin(\lambda)$, with respect to latitude λ, Ω is the planetary rotation rate, and R is the planetary radius. By using the zonal-wind profile measured by Limaye (1986), and taking U to be half the range of wind speeds between minima in the profile, we find the k_β plotted in Fig. 4B.

Although the atmosphere could hypothetically support waves with wavenumbers higher than the Rhines scale, our average spectrum does not show any significant discrete features at higher wavenumbers, signifying a lack of high-frequency periodic structure. We can therefore conclude that the effect on cloud opacities from high-frequency forcing — an example might be highly structured convective overshooting at the base of the stable atmosphere — is relatively weak or nonexistent. Turbulence, not waves, appears to dominate at the smallest scales, which is quite reasonable.

Third, the radius of deformation, L_d, is the principal length scale at which fluctuations produced by baroclinic instability enter the power spectra (Pedlosky 1987, p. 521). L_d is related to the density stratification via $L_d f \approx NH = c$, where N is the Brunt-Väisälä frequency, H is the vertical scale height, c is the phase speed of the fastest gravity-wave mode, and the approximation is valid away from the equator on Jupiter. The midlatitude terrestrial data in the left panel of Fig. 1 show this energy input at $n = 6$. L_d for Jupiter is thought to be ~3,000 km in the stratosphere (Conrath *et al.* 1981) and ~1,800 km in the troposphere (Hammel *et al.* 1995). L_d enters the equations in the context of an inverse wavenumber, *i.e.,* $k^2 + l^2 + L_d^{-2}$, and we have plotted three possible values in Fig. 4C. Panel C's curves are derived from Eq. 3 of Ripa (1983):

$$L_d = \frac{2c}{|f| + \sqrt{f^2 + 2\beta c}}. \tag{2}$$

Lacking definitive information, we take three values for L_d (1,000, 2,000, and 3,000 km) at a latitude of 45° and plot the curves passing through them, assuming constant

c. The shape of these curves would differ from those presented here if c were not constant.

Finally, the quasi-geostrophic approximation, which is involved in the reduction to quasi-two-dimensional fluid dynamics, breaks down if

$$\epsilon = \frac{U}{fL} > 1, \qquad (3)$$

where ϵ is the Rossby number and L is the horizontal length scale. Figure 4D shows the wavenumber corresponding to the length scale where ϵ=1 on Jupiter using the same U as for k_β. We would not expect wavenumbers higher than this value at a given latitude to exhibit the -3 slope of an enstrophy cascade in quasi-two-dimensional turbulence.

These limits are all estimates rather than hard cutoffs, and a factor of 2 in accuracy is the best we can do for most of them (the image quality limit is somewhat better than this).

As discussed earlier, the high-wavenumber fits in Table 3 have power laws near -3, which mimics what would be expected in a kinetic energy spectrum if enstrophy were cascading between wavenumbers ~25 and ~60. Our data reveal a tendency for the slopes to be steeper at higher latitudes. The low latitudes contain more eastward than westward motion, and as a result the westward jet average is steeper than the eastward jet average.

If the empirical correspondence of Travis (1978) is to be believed, then our fits indicate a lack of energy input between wavenumbers ∼25 and ∼60 at most latitudes. Any significant added energy in this range would cause an upscale energy cascade with a -5/3 power law, which would disrupt the observed enstrophy cascade. Thus, the highest discrete wavenumber at which significant energy enters the atmosphere is near 25 under this interpretation. The most likely candidate for the source is baroclinic instability, and this would indicate that $1/L_d$ is somewhere near planetary wavenumber 25, corresponding to $L_d \approx$2,100 km at 45°. We do not see clear evidence for an inertial energy cascade as the low-wavenumber power laws are almost never close to the predicted -5/3 and the confidence level of linear fitting is low.

Our results are partly similar to the conclusions of Mitchell (1982) and Mitchell and Maxworthy (1985). They derived horizontal wind vectors from pairs of Voyager images to calculate the kinetic energy spectrum directly, a distinct advantage over the present work. Their power law exponents are -1.3 and -3, with a breakpoint at planetary wavenumber ∼45. However, the intrinsic uncertainty in wind measurements leads to very noisy spectra. These numbers appear in final form without error estimates, so we cannot quantitatively compare results, but Fig. 3 shows these slopes next to our spectra. We agree with the -3 slope, though it is clear that our breakpoint is not consistent with their location, unless that location has a large error bar. We note that until we compared many nights of data, we were unable to detect the discrete waves that disrupt any low-wavenumber power law in our spectra (see below), and it may be the same effect that yields a first-order behavior of -1.3 rather than -5/3 in their data. The preliminary error analysis of Mitchell (1982) was done in such a way that it might not have detected the influence of discrete waves.

WAVE SEARCH

The only atmospheric waves long enough to be well-resolved by our data are Rossby waves. We envision two means by which a Rossby wave could manifest itself in our data. First, since the zonal winds correspond well with the banded cloud structure (Limaye 1986), a Rossby wave near the edge of a bright or dark band could give rise to a meridional undulation in the location of the edge. Second, since the dynamical thickness of the weather layer containing a Rossby wave varies with the phase of the wave, the local cloud thickness could vary as well, giving rise to an undulating light pattern at a given latitude. Such oscillations are given by the perturbation streamfunction in the dispersion relation derivation of Harrington (1994, Part II Appendix D).

Studying the undulations of the cloud belts at first appears promising. Jupiter's banded cloud patterns provide many regions where clouds end abruptly, so any

Rossby waves strong enough to influence these cloud borders should show up as wiggles in the otherwise-straight interface between a cloud belt and a clear zone. There are other effects that would cause such undulations, however, including passing long-lived vortices and the spread of convected material. Errors in mosaicking and finding the planetary center would further contaminate an edge-location analysis. A wave would also need to perturb a cloud belt by at least one degree of latitude to be seen clearly. Because of these difficulties, we followed the second approach, looking for wave-like intensity variations at a given latitude.

The power spectra show many discrete features, primarily at low wavenumbers. The Lomb normalization tells us the likelihood that a given feature represents an actual periodic signal in the data, as opposed to random noise. Equations 13.8.7 and 13.8.8 of Press *et al.* (1992) state the probability of a power spectrum containing a Lomb-normalized value greater than z by random chance (the false-alarm probability):

$$P(> z) = 1 - (1 - e^{-z})^M \approx M e^{-z}, \tag{4}$$

where M is the number of independent wavenumbers and the approximation is valid for small probabilities. The Nyquist theorem (Eq. 13.8.2 of Press *et al.*) says $M = 180$ for our 1° bins. We wish to expect not to be fooled even once in the entire dataset, and so select a cutoff value for z such that we expect a false alarm only once in at least twice our 121×19 different spectra. Our cutoff is thus $z = 13.6$.

There were 384 locations in our averaged power spectrum image between $\pm 60°$ latitude whose values were greater than our cutoff. We fit sinusoids in the original maps for all 19 nights at the corresponding latitudes and wavenumbers, and derived the amplitude and phase of each wave candidate. Image-processing error exceeds the formal error of the phase fit, so we assigned a phase uncertainty of 1.5 pixels converted to the appropriate angle for a given latitude plus the per-mosaic rotation uncertainty of the particular night (see Paper I).

Long-lived waves propagate at a constant speed, so it would be appropriate to fit a line to the derived phases (see Fig. 5). However, the cyclic nature of phase data prevents the naïve use of linear fitting; some of these data contain enough phases cycles that they appear random when plotted in System III. We therefore iteratively fit the data in a range of rotational reference frames and phase offsets. A fit was good if it had less than $40°$ root-mean-square (RMS) scatter relative to the period (*i.e.,* this number would be $20°$ of planetary phase for an $m = 2$ wave, $5°$ of planetary phase for an $m = 8$ wave, etc.). By fitting the data in the frame of a good fit, we converged to the best fit, usually in one or two iterations. If a candidate wave did not have a frame with better than $40°$ scatter, we doubled the search resolution in both speed and phase. The range of speeds searched was plus or minus 1.5 times the zonal wind plus 15 m/sec. We gave up our search when the resolution reached 5 m/sec in the wave speed. Given the uneven spacing of our 19 nights, finding different speeds that fit the same data well is unlikely below a relatively tight cutoff RMS. We

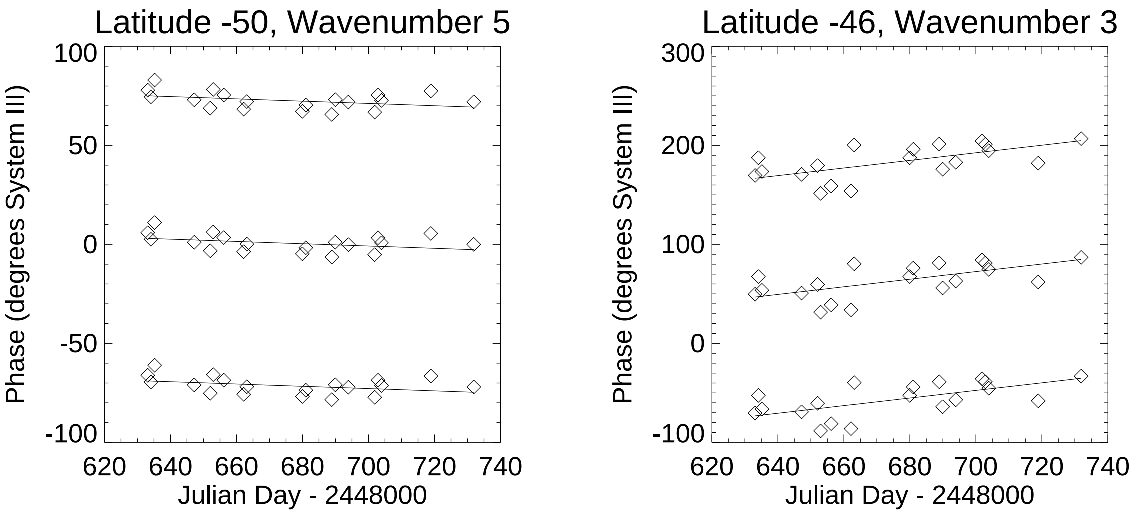

Fig. 5. Linear fits to the best and (nearly) worst wave candidates in Table II (the worst fit has a high velocity that makes the plot difficult to read). Some periodic features in the data propagate with near-linear speeds, making them good wave candidates. The data on each plot are repeated vertically at intervals of one period to show the separation of the data near the center fitted line from the equally-valid data plotted above and below. Of the 384 strong periodic features in the data, only 46 show linear behavior comparable to or better than that of the right panel. Most of these are repetitions of broad features at adjacent latitudes; there are about 24 separate phenomena reported in the table. Some of these appear to follow known features from visible-light images but many remain unidentified.

discovered one such candidate with two fits of similar quality at RMS $\approx 55°$, so Table II presents only those candidates whose RMS is below $40°$.

There is some redundancy in Table II, since some features cross more than $1°$ of latitude. We consider all candidates at the same wavenumber, similar speeds, and adjacent latitudes to be due to the same cause. There are thus about 24 different physical phenomena in the table. Table II additionally shows the zonal wind (from Limaye 1986) at the latitude of a wave candidate, the fitted speed divided by the wind, the mean and standard deviation of Lomb-normalized PSD over the 19 nights,

TABLE II
Linearly Propagating Periodic Features

m	Lat. (°)	Speed (m/s)	RMS (0-360°)	Wind (m/s)	Speed/Wind Ratio	PSD[a]	Above Cutoff (# nights)
2	45	-0.63 ± 0.40	34.97	-0.74	0.85	23 ± 16	11
2	46	-1.76 ± 0.40	39.72	0.68	-2.59	29 ± 17	17
2	48	-3.51 ± 0.39	28.13	26.71	-0.13	47 ± 16	19
2	49	-3.07 ± 0.39	29.17	15.68	-0.20	46 ± 14	19
2	50	-3.53 ± 0.39	36.19	-2.72	1.30	40 ± 14	19
3	-58	3.97 ± 0.37	37.17	-3.30	-1.20	17 ± 8	12
3	-57	4.37 ± 0.37	37.28	-4.15	-1.05	18 ± 10	12
3	-56	4.74 ± 0.37	39.39	-0.41	-11.54	18 ± 12	11
3	-48	-3.92 ± 0.39	35.73	-1.24	3.17	17 ± 10	10
3	-47	-3.12 ± 0.40	37.82	6.80	-0.46	19 ± 12	12
3	-46	-3.98 ± 0.40	39.89	15.67	-0.25	22 ± 13	13
3	-39	6.39 ± 0.41	39.90	5.67	1.13	17 ± 11	12
3	-38	8.36 ± 0.42	30.42	12.62	0.66	17 ± 8	12
3	-37	6.32 ± 0.42	39.24	29.07	0.22	13 ± 5	10
3	-30	3.48 ± 0.43	38.70	23.29	0.15	22 ± 9	16
4	-50	-3.17 ± 0.39	31.13	-6.55	0.48	23 ± 14	14
4	-49	-2.99 ± 0.39	30.36	-7.75	0.39	25 ± 14	15
4	-48	-3.57 ± 0.39	33.53	-1.24	2.89	26 ± 15	14
4	-35	2.73 ± 0.42	35.70	9.14	0.30	14 ± 6	9
4	-34	2.56 ± 0.42	34.89	-2.37	-1.08	14 ± 4	11
4	1	112.46 ± 0.45	36.36	87.13	1.29	20 ± 13	12
4	2	112.20 ± 0.45	38.34	92.21	1.22	21 ± 12	13
4	43	3.50 ± 0.40	32.06	21.81	0.16	26 ± 12	15
4	44	3.78 ± 0.40	32.32	7.66	0.49	24 ± 10	15
4	45	3.82 ± 0.40	37.19	-0.74	-5.17	19 ± 11	11
5	-51	1.56 ± 0.39	34.78	1.59	0.98	15 ± 8	10
5	-50	0.56 ± 0.39	20.65	-6.55	-0.08	18 ± 9	15
5	-49	0.43 ± 0.39	21.01	-7.75	-0.06	20 ± 9	14
5	-48	0.11 ± 0.39	32.12	-1.24	-0.09	18 ± 8	13
5	-32	1.44 ± 0.43	37.05	-15.02	-0.10	14 ± 3	13
5	-31	1.86 ± 0.43	38.69	2.58	0.72	15 ± 3	16
5	-6	99.14 ± 0.45	39.00	114.37	0.87	13 ± 9	7
7	-42	7.08 ± 0.41	29.65	12.69	0.56	26 ± 9	17
7	-41	7.26 ± 0.41	24.95	6.41	1.13	30 ± 9	19
7	-39	7.16 ± 0.41	21.58	5.67	1.26	28 ± 9	17
7	-38	7.59 ± 0.42	39.00	12.62	0.60	22 ± 9	16
7	-37	7.86 ± 0.42	34.35	29.07	0.27	15 ± 7	13
8	-51	1.65 ± 0.39	36.82	1.59	1.04	14 ± 10	10
8	-48	-0.03 ± 0.39	38.75	-1.24	0.03	17 ± 7	13
8	-47	-0.03 ± 0.40	28.33	6.80	-0.00	17 ± 6	11
8	5	103.57 ± 0.45	33.64	101.30	1.02	23 ± 9	16
8	6	103.46 ± 0.45	34.39	102.32	1.01	27 ± 12	17
9	-40	8.22 ± 0.41	38.02	3.70	2.22	14 ± 9	11
9	20	-3.47 ± 0.44	38.15	10.13	-0.34	13 ± 10	7
10	7	105.35 ± 0.45	21.17	103.22	1.02	23 ± 12	16
10	8	104.98 ± 0.45	21.87	101.41	1.04	22 ± 11	16

[a] Average Lomb-normalized power spectral density over 19 nights.

and the number of those nights where the PSD was greater than our cutoff of 13.6.

By searching visually in the map image of 22 March, we have a preliminary identification for some of the candidates. The wavenumber 2-3 candidates are all in regions with clusters of brighter features spaced relatively evenly in longitude. The clustering is more evident in the north than the south. The wavenumber 3 candidate at -30° is very likely related to the lower edge of the GRS; the power spectra there show continua of power. Wavenumber 3 probably propagates linearly because of the bright feature at -35° latitude, 120° away in longitude. At the higher wavenumbers, some of the candidates are due to sequences of individual features that are evenly spaced, or combinations of these and brighter areas of their latitude. Finally, the last candidates are clearly related to the equatorial plumes, being located at latitudes crossed by a sequence of diagonal brightenings. We were unable to identify causes for some candidates in the table. We leave for future work the determination of why there are periodic, propagating brightenings at some latitudes. It is worth noting, again without explanation, that the lower-wavenumber features at latitudes near -47° move with a significant fraction of the zonal wind, but the higher-wavenumber features are all stationary in System III. This precludes a simple Rossby wave interpretation. This description of features is tentative and awaits a more thorough comparison to data at other wavelengths.

With two possible exceptions (wavenumber 3 at -58° and -30° and wavenumber 5 at -51° and -32°), we did not find pairs of candidates at the same wavenumber and speed but at different latitudes. A population of such features would support the banana-cell convection of Hart *et al.* (1986a,b). If the convection underlying the atmosphere follows the banana-cell pattern, any resulting variation in cloud opacity is too weak for us to detect.

CONCLUSIONS

Our power spectra show that Jupiter's cloud opacities follow a power law at planetary wavenumbers above ~25; the exponent is near -3. Variation among latitudes is sometimes larger than the formal errors of the fits, but not out of line with that reported in the literature for the Earth (Julian and Cline 1974). The spectra away from the equator are steeper than those near the equator. Although the theory of atmospheric turbulence has not yet been connected to cloud opacity spectra, our power laws approximate the k^{-3} enstrophy cascade spectrum at high wavenumbers. There is prior observational evidence (Travis 1978) that cloud opacity spectra mimic kinetic energy spectra, in which the enstrophy cascade is found. If this is the case, then our results indicate that there is no significant energy input scale larger than planetary wavenumber ~25, since that would cause an upscale energy cascade with a -5/3 spectrum and would disrupt the power law we observe. We believe it likely that the top of the -3 power law range is associated with L_d, the presumed input scale of baroclinic instability. Although there is not a strong peak at this wavelength, as there is for the Earth's northern hemisphere, detecting it at all suggests that local baroclinic instability is potentially a significant process on Jupiter. If this is the case, then the corresponding value for L_d at 45° latitude is ~2,100 km.

The first search for planetary-scale waves on Jupiter in 5-μm data, conducted by Magalhães *et al.* (1989, 1990) and based on rasterizing Voyager IRIS data, did not detect waves. That study did find periodic thermal features in the upper troposphere and both it and the studies by Deming *et al.* (1989) and Orton *et al.* (1991) detected slowly-moving thermal features in the stratosphere. Significant improvement in spatial and temporal resolution over the spacecraft study have enabled us to report about 24 separate periodic variations in tropospheric cloud opacity that propagate linearly in time. Some of these are due to well-known features, such as the equatorial plumes. Others raise the question of their underlying causes, which we leave for future work. We note that only by incorporating data from all 19 nights of observation and using the Lomb method were we able to identify any propagating waves at all. Our preliminary analysis of the six nights with full longitude coverage (Harrington 1994) did not identify any waves.

Although the appearance of Jupiter did not change on a large scale in our 99 days of observation, its appearance at 4.9 μm has been markedly different in other years. For example, sometimes the rim of the GRS is very bright and the entire latitude band of the GRS is among the brightest and most active on the planet, rather than the darkest. It would be interesting to calculate spectra in the GRS region without an obscuring cloud band. It is possible that the dynamics that cause changes in cloud distribution could also excite wave activity, so it may be worthwhile to perform a search similar to this one when Jupiter's appearance is changing.

ACKNOWLEDGEMENTS

We thank P. Stone, A. Ingersoll, F. M. Flasar, and J. L. Mitchell, R. Pierrehumbert, and two anonymous referees for comments and helpful discussions. Analysis work was funded in part by NASA Planetary Atmospheres grant NAGW-2956. A portion of this work was performed while J. H. held a National Research Council-NASA Goddard Space Flight Center Research Associateship.

REFERENCES

Achterberg, R. K., and F. M. Flasar 1996. Planetary-scale thermal waves in Saturn's upper troposphere. *Icarus* **119**, 350–369.

Allison, M. 1990. Planetary waves in Jupiter's equatorial atmosphere. *Icarus* **83**, 282–307.

Allison M., D. A. Godfrey, and R. F. Beebe 1990. A wave dynamical interpretation of Saturn's polar hexagon. *Science* **247**, 1061–1062.

Batchelor, G. K. 1959. Small-scale variation of convoluted quantities like temperature in turbulent fluid Part 1. General discussion and the case of small conductivity. *J. Fluid Mech.* **5**, 113–133.

Beebe, R. F., A. P. Ingersoll, G. E. Hunt, J. L. Mitchell, and J. P. Müller 1980. Measurements of wind vectors, eddy momentum transports, and energy conversions in Jupiter's atmosphere from Voyager 1 images. *Geophys. Res. Lett.* **7**, 1–4.

Beer, R., and F. W. Taylor 1973. The abundance of CH_3D and the D/H ratio in Jupiter. *Astrophys. J.* **179**, 309–327.

Charney, J. G. 1971. Geostrophic turbulence. *J. Atmos. Sci.* **28**, 1087–1095.

Conrath, B. J., P. J. Gierasch, and N. Nath 1981. Stability of zonal flows on Jupiter. *Icarus* **48**, 256–282.

Danilov, S. D., F. V. Dolzhanskii, and V. A. Krymov 1994. Quasi-two-dimensional hydrodynamics and problems of two-dimensional turbulence. *Chaos* **4**, 299–304.

Deming, D., M. J. Mumma, F. Espenak, D. E. Jennings, T. Kostiuk, G. Wiedemann, R. Loewenstein, and J. Piscitelli 1989. A search for p-mode oscillations of Jupiter: Serendipitous observations of nonacoustic thermal wave structure. *Astrophys. J.* **343**, 456–467.

DOWLING, T. E. 1995. Dynamics of Jovian atmospheres. *Annu. Rev. Fluid Mech.* **27**, 293–334.

DOWLING, T. E., AND A. P. INGERSOLL 1989. Jupiter's Great Red Spot as a shallow water system. *J. Atmos. Sci.* **46**, 3256–3278.

GIERASCH, P. J., A. P. INGERSOLL, AND D. POLLARD 1979. Baroclinic instabilities in Jupiter's zonal flow. *Icarus* **40**, 205–212.

GODFREY, D. A. 1988. A hexagonal feature around Saturn's north pole. *Icarus* **76**, 335–356.

HAMMEL, H. B., R. F. BEEBE, A. P. INGERSOLL, G. S. ORTON, J. R. MILLS, A. A. SIMON, P. CHODAS, J. T. CLARKE, E. DE JONG, T. E. DOWLING, J. HARRINGTON, L. F. HUBER, E. KARKOSCHKA, C. M. SANTORI, A. TOIGO, D. YEOMANS, R. A. WEST 1995. HST imaging of atmospheric phenomena created by the impact of comet Shoemaker-Levy 9. *Science* **267**, 1288–1296.

HARRINGTON, J. 1994. *Planetary Infrared Observations: the Occultation of 28 Sagittarii by Saturn and the Dynamics of Jupiter's Atmosphere.* Doctoral thesis in Earth, Atmospheric, and Planetary Sciences, MIT.

HARRINGTON, J., T. E. DOWLING, AND R. L. BARON 1996. Jupiter's tropospheric thermal emission I: Observations and techniques. *Icarus*, in press.

Copy editor: please replace ''Icarus, in press'' with the actual publication reference in this issue.

HART, J. E., G. A. GLATZMAIER, AND J. TOOMRE 1986a. Space-laboratory and numerical simulations of thermal convection in a rotating hemispherical shell with radial gravity. *J. Fluid Mech.* **173**, 519–544.

Hart, J. E., J. Toomre, A. E. Deane, N. E. Hurlburt, G. A. Glatzmaier, G. H. Fichtl, F. Leslie, W. W. Fowlis, and P. A. Gilman 1986b. Laboratory experiments on planetary and stellar convection performed on Spacelab 3. *Science* **234**, 61–64.

Julian, P. R., and A. K. Cline 1974. The direct estimation of spatial wavenumber spectra of atmospheric variables. *J. Atmos. Sci.* **31**, 1526–1539.

Kunde, V., R. Hanel, W. Maguire, D. Gautier, J. P. Baluteau, A. Marten, A. Chedin, N. Husson, and N. Scott 1982. The tropospheric gas composition of Jupiter's north equatorial belt (NH_3, PH_3, CH_3D, GeH_4, H_2O) and the Jovian D/H isotopic ratio. *Astrophys. J.* **263**, 443–467.

Limaye, S. S. 1986. Jupiter: New estimates of the mean zonal flow at the cloud level. *Icarus* **65**, 335–352.

Magalhães, J. A., A. L. Weir, B. J. Conrath, P. J. Gierasch, and S. S. Leroy 1989. Slowly moving thermal features on Jupiter. *Nature* **337**, 444–447.

Magalhães, J. A., A. L. Weir, B. J. Conrath, P. J. Gierasch, and S. S. Leroy 1990. Zonal motion and structure in Jupiter's upper troposphere from Voyager infrared and imaging observations. *Icarus* **88**, 39–72.

Mitchell, J. L. 1982. The Nature of Large-Scale Turbulence in the Jovian Atmosphere. JPL Publication 82-34, Jet Propulsion Laboratory, Pasadena, CA.

Mitchell, J. L., and T. Maxworthy 1985. Large-scale turbulence in the Jovian atmosphere. In *Turbulence and Predictability in Geophysical Fluid Dynamics and Climate Dynamics*, pp. 226–240. Tipografia Compositori, Bologna, Italy.

ORTON, G. S., A. J. FRIEDSON, J. CALDWELL, H. B. HAMMEL, K. H. BAINES, J. T. BERGSTRALH, T. Z. MARTIN, M. F. MALCOM, R. A. WEST, W. F. GOLISCH, D. M. GRIEP, C. D. KAMINSKI, A. T. TOKUNAGA, R. BARON, AND M. SHURE 1991. Thermal maps of Jupiter: Spatial organization and time dependence of stratospheric temperatures, 1980 to 1990. *Science* **252**, 537–542.

PEDLOSKY, J. 1987. *Geophysical Fluid Dynamics*, 2^{nd} ed. Springer Verlag, New York.

PIERREHUMBERT, R. T. 1992. Spectra of tracer distributions: A geometric approach. In *Nonlinear Phenomena in Atmospheric and Oceanic Sciences*, G. Carnevale and R. T. Pierrehumbert, eds. Springer Verlag, New York, pp. 27–46.

PIERREHUMBERT, R. T. 1994. Tracer microstructure in the large-eddy dominated regime. *Chaos, Solitons, and Fractals* **4**, 1091–1110.

PRESS, W. H., S. A. TEUKOLSKY, W. T. VETTERLING, AND B. P. FLANNERY 1992. *Numerical Recipes in C: The Art of Scientific Computing*, 2^{nd} ed. Cambridge University Press.

RHINES, P. B. 1979. Geostrophic turbulence. *Ann. Rev. Fluid Mech.* **11**, 401–441.

RIPA, P. 1983. General stability conditions for zonal flows in a one-layer model on the β-plane or the sphere. *J. Atmos. Sci.* **126**, 463–489.

SADA, P. V., R. F. BEEBE, AND B. J. CONRATH 1996. Comparison of the structure and dynamics of Jupiter's Great Red Spot between the Voyager 1 and 2 encounters. *Icarus* **119**, 311–335.

Saffman, P. G. 1971. On the spectrum and decay of random two-dimensional vorticity distributions at large Reynolds numbers. *Studies in Appl. Math.* **50**, 377–383.

Shepherd, T. E. 1987. Rossby waves and two-dimensional turbulence in a large-scale zonal jet. *J. Fluid Mech.* **183**, 467–509.

Terrile, R. J. 1978. *High Spatial Resolution Infrared Imaging of Jupiter: Implications for the Vertical Cloud Structure from Five-Micron Measurements.* Doctoral thesis, California Institute of Technology.

Tessier, Y., S. Lovejoy, and D. Schertzer 1993. Universal multifractals: Theory and observations for rain and clouds. *J. Appl. Meteorology* **32**, 223–250.

Travis, L. D. 1978. Nature of the atmospheric dynamics on Venus from power spectrum analysis of Mariner 10 images. *J. Atmos. Sci.* **35**, 1584–1595.

West, R. A. D. F. Strobel, and M. G. Tomasko 1986. Clouds, aerosols, and photochemistry in the Jovian atmosphere. *Icarus* **65**, 161–217.